Forgotten treasures in the HST/FOC UV imaging polarimetric archives of active galactic nuclei

T. Barnouin, F. Marin, E. Lopez-Rodriguez

A&A, 692, A178 (2024)
https://doi.org/10.1051/0004-6361/202451105

Astronomy & Astrophysics

Forgotten treasures in the HST/FOC UV imaging polarimetric archives of active galactic nuclei

II. Mrk 463E

T. Barnouin[1,⋆], F. Marin[1], and E. Lopez-Rodriguez[2]

[1] Université de Strasbourg, CNRS, Observatoire astronomique de Strasbourg, UMR 7550, F-67000 Strasbourg, France
[2] Kavli Institute for Particle Astrophysics & Cosmology (KIPAC), Stanford University, Stanford, CA 94305, USA

Received 13 June 2024 / Accepted 11 November 2024

ABSTRACT

Context. The Mrk 463 system is known to host two powerful sources that are separated by about 4 kpc, which were both identified as active galactic nuclei (AGN). This makes the Mrk 463 system a unique laboratory for studying the geometry and dynamics of galaxy merging and its relation to AGN duty cycles.
Aims. The eastern nucleus, Mrk 463E, is the brighter of the two and thus a prime target for a polarimetric study. It is classified as a Seyfert 2 galaxy, meaning that high polarization degrees from scattering off electrons and dust in the polar winds are expected.
Methods. In the continuity of our series of papers, we reduced archived and previously unpublished polarization observations obtained with the Faint Object Camera on board the Hubble Space Telescope to obtain a high-resolution near-ultraviolet polarization map of the Mrk 463E nuclei. We coupled this map to near-infrared and X-ray observations to obtain a clear picture of the geometric arrangement of matter around the core of Mrk 463E.
Results. We found that the nucleus location is farther south of the optical peak flux than previously estimated. The strongly polarized conical wind has a half-opening angle of ∼15° and displays three main periods of mass ejection. Its polarization allowed us to estimate the AGN inclination toward the observer (∼55°). Finally, our maps revealed a streamer connecting Mrk 463E and Mrk 463W, with a tentative detection of a large kiloparsec-scale ordered magnetic field connecting both galaxies.
Conclusions. This unpublished observation finally offered more than the original proposal asked for and allowed us to derive tight geometric and dynamical constraints for Mrk 463E. High-resolution radio maps and infrared polarimetry are now necessary to further study the jet and the newly discovered streamer.

Key words. polarization – instrumentation: polarimeters – methods: observational – astronomical databases: miscellaneous – galaxies: active – galaxies: Seyfert

1. Introduction

It is now quite widely accepted that massive galaxies host a supermassive black hole (SMBH) at their center. The most recent observations from the Event Horizon Telescope provided powerful evidence for their existence in the nearby galaxy M87 (Event Horizon Telescope Collaboration 2019), as well as in the center of our own galaxy (Event Horizon Telescope Collaboration 2022). However, their formation and growth remains difficult to trace, and this is even more so when the parallel evolution of their host galaxy is taken into account (Di Matteo et al. 2005). Massive black hole mergers and powerful accretion phases that cause the so-called active galactic nuclei (AGN) are the main processes with which we explain SMBH growth (Di Matteo et al. 2005; Treister et al. 2012). However, when they are taken separately, these growth models remain too slow for both galactic and cosmological simulations to explain the observed SMBH masses with respect to their host galaxy age (Capelo et al. 2017; Volonteri et al. 2022). Both processes need to occur simultaneously in the lifetime of a black hole for it to become supermassive. The best place to search for concurrent merging and accretion are probably ultra-luminous infrared galaxies (ULIRG, Sanders et al. 1988), which are thought to be the ongoing phase or the remnant of a merging process that is able to bring much dust and gas to the vicinity of their central SMBH (Barnes & Hernquist 1991; Hopkins et al. 2006). This could trigger an AGN phase and lead to intense SMBH growth at the same time (Treister et al. 2012).

Mrk 463 is a nearby ∼224 Mpc (in standard ΛCDM cosmology) merging system consisting of two nuclei, Mrk 463E (east, $z = 0.05132$; Lavaux & Hudson 2011) and Mrk 463W (west, $z = 0.05055$; Abazajian et al. 2009), separated by $3.8'' \pm 0.01''$. This separation corresponds to a projected distance of ∼4.1 kpc. Observations in the radio (Neff & Ulvestad 1988; Mazzarella et al. 1991), [OIII], and [NII] bands (Hutchings & Neff 1989; Chatzichristou & Vanderriest 1995) were used to study the interconnected nuclei and revealed tidal tails from a recent violent interaction as well as evidence for the ongoing merging of the two galaxies (Hutchings & Neff 1989; Mazzarella et al. 1991). High-resolution 6 cm radio observations of the eastern nuclei, Mrk 463E, revealed a small-scale jet ($0.05''$ to $1.5''$) along a position angle (PA) of ∼11° (Neff & Ulvestad 1988). At 20 cm, Mazzarella et al. (1991) observed extended but isolated emission sources situated $18''$ (∼20 kpc) south and $4''$ (∼5 kpc) north of Mrk 463E, without optical or IR counterparts. They are not connected to the bright

⋆ Corresponding author;
thibault.barnouin@astro.unistra.fr

radio emission of the nucleus, but since they are located along the same axis as the small radio jets and have characteristics of classic radio lobes, they were associated with Mrk 463E as weak radio lobes. The jets associated with Mrk 463E can be extended up to another emission region as far as ∼12 kpc northwest of the nuclei (Neff & Ulvestad 1988; Mazzarella et al. 1991). This extended radio emission and its strong luminosity density place Mrk 463E in the classification between Seyfert and radio galaxies.

Because it was early identified as a type 2 Seyfert galaxy (Shuder & Osterbrock 1981), the eastern nucleus of Mrk 463 has been the focus of polarization studies that aimed to determine whether the AGN fits the unified model (Antonucci 1993). Miller & Goodrich (1990) discovered broad emission lines in its polarized spectrum, which proved the presence of a type 1 nucleus behind some obscuring material. Broad (full width at half-maximum ∼2750 km·s^{-1}) Hβ and Hα Balmer lines were detected in polarized flux, with an intrinsic polarization degree of 10% and an electric vector polarization angle of 85° (after correction for interstellar polarization), which was comparable to the other archetypal Seyfert-2 AGN NGC 1068 (Antonucci & Miller 1985; Tran 1995a,c). Miller & Goodrich (1990) also found a strong 5500 Å continuum linear polarization of 7.7% with a polarization angle of ∼82°, almost perpendicular to the radio PA (∼4°; Unger et al. (1986) and Neff & Ulvestad 1988). Similarly to NGC 1068 (Antonucci & Miller 1985), the Mrk 463E ionization cones spread along the radio axis, and their illumination by the central engine can easily explain these polarization levels and angles. However, the detected narrowing of the [OIII] and [OII] emission lines in the polarized spectrum indicated unresolved geometric or dynamic features (Miller & Goodrich 1990; Tran 1995c) and sparked new studies of Mrk 463E at higher spatial resolutions.

High-resolution imaging of the eastern nucleus in the optical band was obtained with the Planetary Camera (PC) on board the Hubble Space Telescope (HST) in July 1991. This observation led to the discovery of a subarcsecond-scale jet-like structure around the nucleus (Uomoto et al. 1993). While similar in morphology to the optical jets of M87 and 3C 273, the radio emission in Mrk 463E is positioned just beyond the end of this optical jet. The optical and radio emission are not correlated, and therefore, the observed optical emission from this jet cannot be synchrotron in nature. Because the axis of this polar structure is almost perpendicular to the detected continuum polarization, Uomoto et al. (1993) suggested that it was the scattering site that allows the observation of the hidden Seyfert-1 galaxy, which produces the polarized spectrum observed by Miller & Goodrich (1990). A follow-up observation using the Faint Object Camera (FOC) on board HST was performed in May 1996 to verify this prediction. To this day, these high-quality data were never reduced, analyzed, or published, despite some preliminary announcements by Tremonti et al. (1996).

The study of the Mrk 463 system continued at higher energies, especially because the spectral type and true AGN nature of the western nuclei were never confirmed (Shuder & Osterbrock 1981; Neff & Ulvestad 1988). A Chandra high-energy (2–8 keV) imaging analysis of the Mrk 463 system revealed two unresolved X-ray sources coincident with the two nuclei detected in the radio and IR (Bianchi et al. 2008). An X-ray spectral analysis using Chandra, XMM-Newton and NuSTAR data showed that Mrk 463W is a Compton-thin obscured AGN ($n_{\rm H} \leq 10^{24}$ at/cm^2) with a low bolometric to X-ray luminosity ratio ($\kappa_{2-10{\rm keV}} \sim 1-3$), suggesting a low Eddington ratio ($<10^{-3}$; Yamada et al. 2018). Hence, Mrk 463W most probably is in an early phase of AGN activity triggered by the merger event. The same analysis showed for the eastern nucleus that its intrinsic spectrum is X-ray weak (with respect to its UV luminosity), but is associated with a high Eddington ratio ($\lambda_{\rm Edd}$ = 0.4−0.8; Bianchi et al. 2008; Yamada et al. 2018). This would suggest a Compton-thin obscured AGN with a rapidly growing SMBH. The recent merger event could have triggered efficient gas fueling onto the SMBH without deeply burying the nuclei in gas and dust.

It is thus evident that because of its distance, luminosity, and recent history, the Mrk 463 system makes a unique laboratory for studying AGN evolution and SMBH growth. A violent interaction between its two nuclei probably triggered their AGN phase, as observed from the radio to the X-rays. Some high-resolution archival data still remain to be analyzed to complete and better understand the interaction of the regions, the nature of the bright subarcsecond-scale optical jet-like structure in Mrk 463E, and the arrangement of matter around this nucleus. In this second paper of our series about the archival HST/FOC data, we therefore reduce and analyze for the first time a near-ultraviolet (NUV) imaging polarimetry observation of the scattering regions of Mrk 463E as requested in 1995, to verify the prediction of Uomoto et al. (1993). In Sect. 2, we present the observation and data reduction techniques. The reduced polarization map is analyzed in detail in Sect. 3, making use of the high spatial resolution of the instrument to map several specific regions around the nucleus. Sect. 4 places this observation in a multiwavelength context to better highlight the different processes at play and understand the nature of the jet-like structure. The results of this analysis are discussed in Sect. 5. Sect. 6 summarizes our findings.

2. Observation and data reduction

Mrk 463E was observed by the HST/FOC on May 10, 1996 (program ID 5960). This observation was requested as a follow-up of the previous HST/PC observation that was analyzed and published in Uomoto et al. (1993). Its goal was to inspect in NUV light the subarcsecond jet-like structure discovered in the optical and determine whether it indeed is a scattering site. This observation was made in the f/96 mode without the zoom. It resulted in pixels with a size of 0.014″ × 0.014″ for a 7″ × 7″ field of view (FoV). It used the F342W filter centered around 3404 Å for a total exposure time of 10,748 seconds, 11 300 seconds, and 10 748 seconds through the POL0, POL60, and POL120 filters, respectively. The observation products were stored in different flavors of calibration in the MAST/HST legacy archives of the FOC: either raw uncalibrated data, geometry- and exposure-corrected data, or geometry-, exposure-, and flatfield-corrected data. The data were retrieved and reduced as described in the first paper of our series (Barnouin et al. 2023). We refer to this paper for an in-depth explanation of the reduction steps and definition of the uncertainties (Sect. 2.7 in the aforementioned paper, σ_I and σ_P) that are used in the following analysis. All reported polarization degrees were corrected for bias (Simmons & Stewart 1985).

For this observation, the FoV of the FOC instrument was centered on the eastern nucleus, which places the western nucleus just outside of the image. A quick analysis revealed little to no contamination of light from Mrk 463W: Only part of an extended source can be seen in the bottom right corner of the instrument FoV (as seen in Fig. 1). The imaging capacities of the HST/FOC allowed us to spatially distinguish the direct emission from the western nucleus from the eastern nucleus emission, and we analyzed them separately. For the analysis of Mrk 463E in the

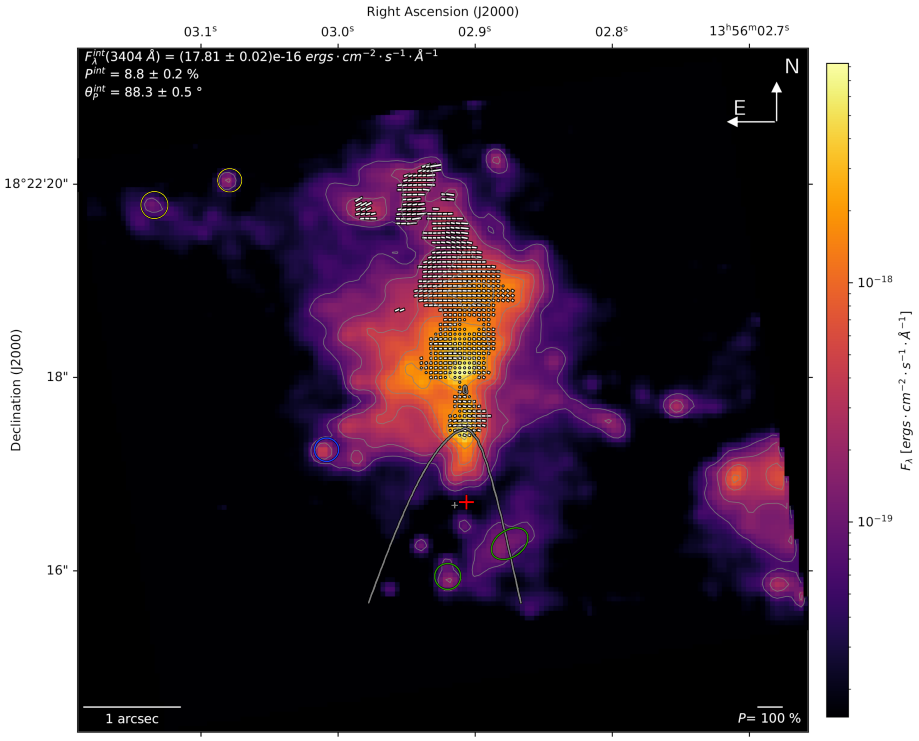

Fig. 1. HST/FOC observation of Mrk 463E resampled to pixels of 0.05″×0.05″. The intensity is color-coded in erg cm^{-2} s^{-1} Å^{-1}. The polarization vectors are displayed for Conf$_P$ ≥ 99%. The dark gray contour and cross, as well as the red cross, show our estimates for the nucleus location and are discussed in Sect. 3.1 and Appendix B. The flux density contours are displayed for 0.8%, 2%, 5%, 10%, 20%, and 50% of the maximum flux density. The top left corner values are integrated over the whole FOC FoV (7″ × 7″): $F_\lambda^{\rm int}$ = (17.81 ± 0.02) × 10^{-16} ergs cm^{-2} s^{-1} Å^{-1} with $P^{\rm int}$ = 8.8 ± 0.2% and $\Psi^{\rm int}$ = 88.3 ± 0.5°. The circled spots are discussed in Sect. 3.1.

following, the extended emission from Mrk 463W was cropped out of the region of interest.

The long exposure time through each polarized filter allowed us to obtain statistically significant measurements through our reduction pipeline: In the resampled 256×256 pixel resolution of the FOC (Nyquist sampling of the native 512 × 512 pixel image) and without smoothing, we obtained a flux detection (at ≥3σ_I) in 33.8% of the pixels, 0.03% of which have a polarization detection (≥3σ_P), amounting to 6 pixels. The retrieved data were not deconvoluted with a Richardson-Lucy algorithm, in contrast to what was done in Uomoto et al. (1993), because we wished to study the diffuse emission from the narrow-line region (NLR) and because of the native high signal-to-noise ratio (S/N) per pixel in the region of interest. In the following section, we thus present an analysis of the polarization map rebinned to pixels with a size of 0.05″ × 0.05″, that is, 3.5 times the native pixel size, and smoothed with a bidimensional Gaussian filter with a full width at half-maximum of 0.10″, that is, twice the resampled pixel size. Unlike the first paper of this series, the polarization vectors are shown for a confidence level on the polarization degree (Conf$_P$) greater than 99%. For every measure, the confidence level was computed for two degrees of freedom: For the normalized Stokes Q and U fluxes (see Appendix A for details). We integrated inside a region of interest or selected aperture on the Stokes I, Q, and U fluxes before we computed the polarization degree and the angle and bias correction.

3. Polarization analysis

3.1. The FOC polarization map

Fig. 1 shows the polarization map overlaid on the total intensity image. The polarization vectors are displayed for Conf$_P$ ≥ 99%, their length is proportional to their polarization degree, and they are oriented according to their electric vector polarization angle, from north to east, following the IAU convention (IAU 1973). The total flux density image is dominated by two hot spots in the flux density on a north-south axis, whose centers are separated by ∼0.67 kpc (projected distance). These large hot spots are connected by a narrow flux density column, as if an external constraint created a physical bottleneck between the two extended flux density spots. Intense emission surrounds these two hot spots and forms a well-contrasted large-scale cone-shaped region. This geometry was observed for many other Seyfert AGNs (see, e.g. Miller et al. 1991; Wang et al. 2024; Wilson 1996). This bicone (or hourglass-shaped) structure is known to be associated with the NLR, emerging from the (unresolved) vicinity of the black hole and extending hundreds of parsecs along the polar axis of the AGN, often revealed in [O III] mapping (see, e.g. Walker 1968; Oke & Sargent 1968; Mullaney et al. 2013). Because [O III] is a forbidden line, it is able to trace the kinematics in the NLR, which was measured to be about 300 km s^{-1} to 600 km s^{-1} by Treister et al. (2018) in the case of Mrk 463E. The highest velocities are reached in a small region northeast of the northern cone, with an apparent different flow direction than the NLR itself. In our map, a few ovoid clumps with a stronger polarization than the NLR seem to escape the wind in the northeast direction, which strengthens the idea that the NLR is a dynamical region. The southern part of the Mrk 463E bicone is not visible. It is likely hidden behind the host galaxy plane (see Sec. 4.1 for further details).

A second less extended emission originating from the western nucleus, Mrk 463W, is visible at the southwest border of the FoV. As we lack a good part of the emission from Mrk 463W, we cannot infer the geometrical aspect and emission characteristics of the region that appears in this observation. We report no detectable polarization from Mrk 463W: The polarization features in the western nucleus remain below 2σ_P and cannot be dissociated from noise. However, a stream-like feature extends from the base of the observed polar wind of Mrk 463E in an elliptical arc in the general direction of Mrk 463W. This arc, visible in total intensity (see Fig. 1), has no Conf$_P$ ≥ 99% polarized counterparts (see Fig. 2; see Sect. 5.1 for further details about this arc-like structure).

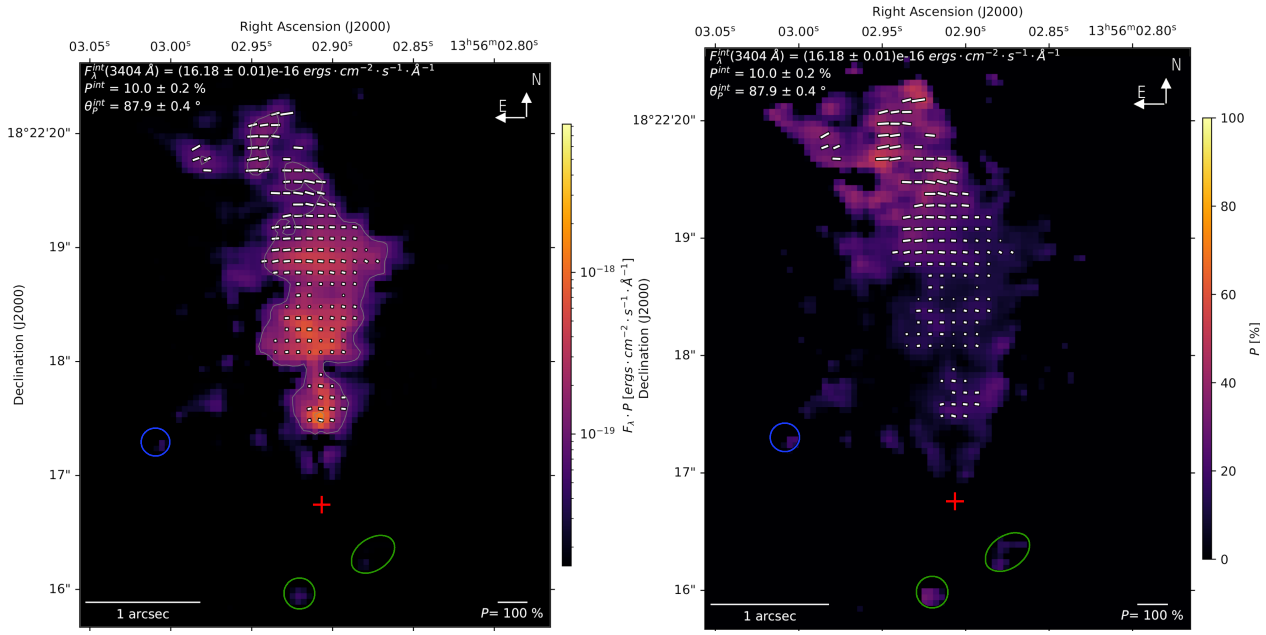

Fig. 2. Cropped polarized flux density (left) and polarization degree (right) maps highlighting the northern scattering region of Mrk 463E. The red cross shows our estimate for the nucleus location. The circled spots are discussed in Sect. 3.1. For better visibility, we only display every other vector.

In the polarized flux density map shown in the left part of Fig. 2, the aforementioned conic wind and ovoid clumps account for almost all of the polarized flux density. The cone appears much narrower in polarized flux density (half-opening angle of ∼15°) than what can be seen in total intensity (half-opening angle of ∼36°), both reported in Fig. 3. This is similar to what has been observed in NGC 1068, for which the ionization cone appears to be much narrower in polarized flux density (Miller et al. 1991). We used both of these cone delimitations to estimate the nucleus location. It is displayed as a red cross in Figs. 1, 2, and 3. The coordinates of the nucleus according to our polarization map are 13h56m02.91s, 18°22′16.6″. A second estimate of the nucleus location, deduced from the centrosymmetric pattern of the polarization vectors onto the northern polar outflow and inspired by the method of Kishimoto (1999), agrees with this estimate and is presented in Appendix B.

In polarized flux density, a bottleneck-like feature appears between the two hot spots. This apparent bridge between the extended clumps in the NLR could come from the scattering of the UV continuum from the nuclei on material in the parsec-scale radio jet at position angle 180° (Mazzarella et al. 1991; Kukula et al. 1999). This could be investigated by correlating our NUV polarization map to high-resolution radio maps. Just outside the conical wind, ∼1.5 kpc east of the southern hot spot, a spherical clump (circled in blue in Figs. 1 and 2) appears in both total and polarized flux density with $P = 19.8 \pm 4.9\%$ at $\Psi = 76.2 \pm 7.1°$. Two other spherical clumps (circled in yellow in Fig. 1) are visible in total intensity and polarization east of the northern end of the polar wind, lying at ∼2.8 kpc and ∼3.5 kpc east of the major clumps north of the NLR cone, with $P = 37.4 \pm 13.8\%$ at $\Psi = 148.4 \pm 10.4°$ and $P = 11.4 \pm 5.9\%$ at $\Psi = 56.5 \pm 14.8°$, respectively. As both values are below $3\sigma_P$, this only indicates a possible polarization of the clumps and therefore has to be taken with caution. South of the wind, two small knots (circled in green in Figs. 1 and 2) appear in polarization, at ∼0.6 kpc southwest and ∼1 kpc southeast of the vertex of the wind cone with $P = 17.0 \pm 3.3\%$ at $\Psi = 126.2 \pm 5.5°$ and $P = 24.4 \pm 4.3\%$ at $\Psi = 77.0 \pm 5.1°$, respectively.

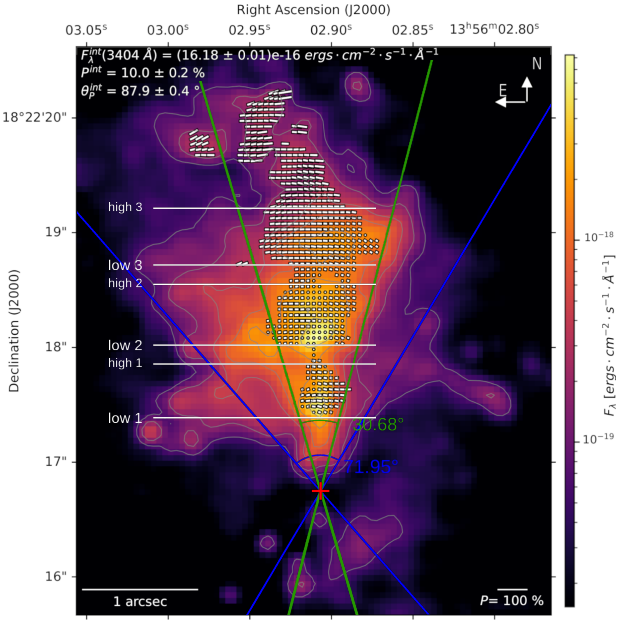

Fig. 3. Total intensity NUV map from the HST/FOC cropped around the northern winds of Mrk 463E. The blue and green lines represent the total opening angle for the wind cones as seen in total intensity (71.95°) and polarized flux (30.68°), respectively. The red cross shows our estimate for the location of the nucleus.

All these features can be seen in the polarization degree map in the right part of Fig. 2. This map reveals that the polarization inside of the NLR does not exceed 20%, and it drops to zero around the center of the bottleneck structure. North of the NLR, the clumps show a polarization degree above 30% that increases to almost 50% as they recede from the first two arcseconds around the supposed position of the SMBH.

The orientation of the centro-symmetric polarization pattern inside of the polar wind is coherent with the scattering of UV

continuum from an unresolved source south of the cone. This centro-symmetric pattern was also observed for IC 5063 and NGC 1068 in the previous paper of this series (Barnouin et al. 2023) and reproduced the results of previous imaging polarimetry of NGC 1068. It indicates the location of the nucleus based on this circular pattern (Capetti et al. 1995; Kishimoto 1999). We also note that the polarization angle of the escaping clumps northeast of the wind also indicate the same unresolved source that is south of the cone. The polarization angle pattern clearly proves the intuition of Uomoto et al. (1993), who suggested that the base of the extended polar wind of Mrk 463E acts like a mirror, allowing the observation of the hidden broad emission lines in polarized flux density.

3.2. Comparison with a previous polarimetric analysis

Integration over the whole HST/FOC FoV yields a total flux density of $F_\lambda^{\rm int} = (17.81 \pm 0.02) \times 10^{-16}$ ergs cm^{-2} s^{-1} Å^{-1}, with a polarization degree $P^{\rm int} = 8.8 \pm 0.2\%$ and a global polarization position angle $\Psi^{\rm int} = 88.3 \pm 0.5°$. Cropping the observation to remove Mrk 463W, as shown in Figs. 2 and 4, yields $F_\lambda^{\rm int} = (16.18 \pm 0.01) \times 10^{-16}$ ergs cm^{-2} s^{-1} Å^{-1}, $P^{\rm int} = 10.0 \pm 0.2\%$ and $\Psi^{\rm int} = 87.9 \pm 0.4°$. This cropped polarization map that only shows Mrk 463E was used in the following analysis. Finally, integrating only the contribution from the polar wind (including the escaping clumps) yields a polarization degree $P^{\rm int} = 12.5 \pm 0.2\%$ at position angle $\Psi^{\rm int} = 87.5 \pm 0.3°$, which clearly indicates that most of the polarized flux density comes from reprocessing in the winds. In all cases, the polarization angle is perpendicular to the ∼4° radio position angle measured by Unger et al. (1986) and Neff & Ulvestad (1988), as expected for a type 2 AGN.

We compared our HST/FOC map to previous observations. It is a fairly common target, and a plethora of spectropolarimetric data exists. A direct flux-to-flux comparison with Watanabe et al. (2003) validated the flux density measured by HST: The authors measured a total flux density of 6.8×10^{-15} ergs cm^{-2} s^{-1} Å^{-1} at 5400 Å in a 3″ extraction window in 2001, February 21. The slight difference between the two fluxes is easily explained as due to the different wavelength windows (the total flux spectrum of Mrk 463 rising to the blue) and also to the seeing conditions on Earth (1.3−1.4″) and (the lack of) in space. Watanabe et al. (2003) acquired polarized spectra of Mrk 463E from 4600 Å to 25 000 Å, and their polarization degree and angle (10.4% and 82°) at 5400 Å agree well with our measurements at 3404 Å. This indicates that electron scattering could be at work here because the polarization is roughly independent of the wavelength, as expected for electron scattering versus dust scattering, which would generally increase with decreasing wavelength (Miller et al. 1991), but the lack of error bars for the measurements of Watanabe et al. (2003) hamper a strong conclusion.

Young et al. (1996) obtained optical and near-IR broadband polarimetric observations of Mrk 463E using the 3.8m United Kingdom Infrared Telescope (UKIRT) and a 5.0″ aperture. They reported $P = 6.48 \pm 0.5\%$ at $\Psi = 86 \pm 2°$ in the U band and $P = 5.78 \pm 0.28\%$ at $\Psi = 88 \pm 1°$ in the V band, which both agree with our full FoV polarization at 3404 Å which benefited from less unpolarized light contamination. Mrk 463E was also observed both in imaging polarimetry and spectropolarimetry with the 3m Shane telescope at the Lick observatory. The spectropolarimetric analysis was performed through a north-south oriented 2.4″ wide and 10″ long slit (see Fig. 30 in Tran 1995b) and was presented in Miller & Goodrich (1990) and Tran (1995a). They

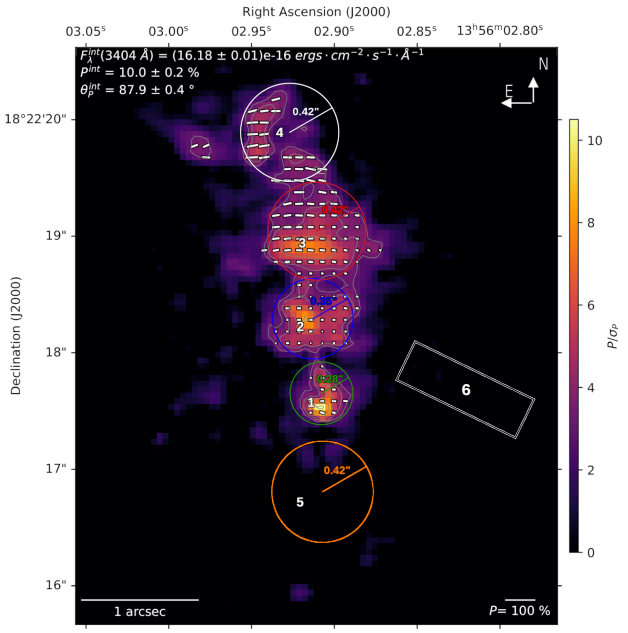

Fig. 4. Knots in the north polar wind. For better visibility, we only display every other vector. The sixth region corresponds to a simulated slit aperture of 0.35″ × 1.15″ along the the stream-like feature that can be observed in Fig. 1, and which is discussed in Sect. 5.1.

obtained a continuum polarization of $P = 7.6\%$ at $\Psi = 85°$ in the 3200–7400 Å (they also reported a broad line polarization of $P = 10\%$ at $\Psi = 84°$). We simulated this slit by integrating the I, Q, and U Stokes fluxes inside a 2.4″ wide and 7″ long slit (limited by the 7″ × 7″ FoV of the HST/FOC) oriented north-south and centered on the [O III] maximum flux. We report an integrated flux density around 3404 Å of $F_\lambda^{\rm int} = (12.57 \pm 0.01) \times 10^{-16}$ ergs cm^{-2} s^{-1} Å^{-1} and a polarization degree of $P = 10.8 \pm 0.2\%$ at position angle $\Psi = 87.6 \pm 0.4°$, which is also compatible with the previously reported optical polarization.

3.3. Region-specific polarization analysis

The unmatched imaging resolution of the HST/FOC in the NUV band allowed us to perform region-specific polarimetric studies. In the following, we use simulated apertures and slits to obtain integrated polarization characteristics for selected regions. The regions for aperture integration are shown in Fig. 4 overlaid on the S/N map in polarization degree, and the contribution from Mrk 463W is cropped out. This particular map allowed us to select regions with a high polarization degree, based on the most significant polarization detection. We report the integrated values for each region for the flux density, polarization degree, and angle in Table 1.

Regions 1, 2, and 3 correspond to clumpy structures located inside of the northern polar wind showing highly polarized flux densities (see Fig. 2). As we probed clumps farther away from the nucleus, we moved along the polar axis and found that the clumps conserve a polarization angle that is coherent with perpendicular scattering. The slightly different polarization angle $\Psi^2 \simeq 87.6°$ of region 2 with respect to regions 1 and 3 can easily be explained by the fact that the center of the polarized flux knot is displaced east of the polar axis.

Region 4 was selected to focus on the escaping clumps northeast of the wind. The integrated polarization shows a polarization

angle of $\Psi^4 \simeq 92.5°$, which is a few degrees higher than regions 1 to 3 in the cone, but still consistent with diffusion of the continuum from the nucleus. These clouds are also characterized by a strong polarization degree of $P^4 \simeq 34\%$. This could be due to a variety of reasons, such as less perturbed medium than in the cone, lower obscuration along the line of sight, or a higher albedo, which are indistinguishable in this context.

Region 5 corresponds to the location of the hidden southern polar cone. While it is not clear at this stage whether the wind is simply absent or obscured (see Sect. 4.1 for further discussion), we wished to verify whether polarization could be detected here. We find a low but statistically significant ($\sim 5.5\sigma_P$) polarization degree associated with a polarization angle perpendicular to the jet direction. It indicates that there is a scattering region, likely in the form of a wind (or at least clumps), but the total flux signal seems highly attenuated, probably by dust absorption.

The stream-like feature that extends from Mrk 463E toward Mrk 463W and is only visible in total intensity is the focus of region 6. We simulated a 0.35″ wide and 1.15″ long slit, oriented 67° east of north, to integrate the Stokes fluxes especially along the hypothetical stream. Unfortunately, the detected polarization is below $3\sigma_P$ and we cannot make strong claims here without further observations. Nevertheless, if the structure is real, we have indications for a polarization degree $P^6 = 3.8 \pm 1.9\%$ at an electric polarization angle $\Psi^6 = 133.4 \pm 14.3°$ (with an 89% confidence level for two degrees of freedom on the Stokes Q and U fluxes). We discuss these results in Sect. 5.1.

Table 1. Integrated flux density and polarization over several regions of interest.

Region	Flux density (10^{-17} ergs cm^{-2} s^{-1} Å^{-1})	P (%)	PA (°)
Full FoV	178.10 ± 0.20	8.8 ± 0.2	88.3 ± 0.5
Cropped FoV	161.80 ± 0.10	10.0 ± 0.2	87.9 ± 0.4
Cone+clumps	105.70 ± 0.10	12.5 ± 0.2	87.5 ± 0.3
2.4″ × 7″ slit	125.70 ± 0.10	10.8 ± 0.2	87.6 ± 0.4
1	14.77 ± 0.03	12.8 ± 0.4	85.3 ± 0.8
2	35.25 ± 0.05	11.0 ± 0.3	87.6 ± 0.6
3	19.16 ± 0.03	17.6 ± 0.3	84.7 ± 0.5
4	3.30 ± 0.02	33.9 ± 0.9	92.5 ± 0.8
5	2.21 ± 0.02	6.0 ± 1.1	99.3 ± 5.3
6	0.96 ± 0.01	3.8 ± 1.9	133.4 ± 14.3

Notes. The integration regions are displayed in Fig. 4. The reported polarization degrees are corrected for bias (Simmons & Stewart 1985).

4. Multiwavelength analysis

4.1. Correlation with HST/WFPC2 near-IR observation

The Mrk 463 system was observed using the Wide Field Planetary Camera 2 (WFPC2) on board HST in November 1995 as part of a sample of ten near infrared quasars (Proposal ID 5982). The binary system was observed through the F814W filter, centered around 7996 Å with a bandwidth of 646 Å. The results of this observation were published in Sanders & Mirabel (1996). While the WFPC2 has a spatial resolution similar to that of the FOC (pixels with a size of 0.0455″ × 0.0455″), it benefits from a much wider FoV of 36″×36″. We thus decided to take advantage of the WFPC2 observation of Mrk 463E in order to better understand the geometric configuration of matter around the nucleus, as well as its composition.

We downloaded and reduced the WFPC2 data, and we overlay in Fig. 5 the FOC total intensity (gray contours) and polarization (white vectors) maps on the near-infrared (NIR) total intensity map taken with the F814W filter. Both maps were aligned on similar-looking punctual and extended features, as shown in the zoomed box in the right part of Fig. 5. The wider FoV of WFPC2 allowed us to observe both nuclei at once and to better assess the contribution of the western object to the FOC image. This simple overlay shows that the Mrk 463E maximum intensity regions in the NUV and NIR do not overlap, with the NIR peak just south of the NUV peak. We also note that the stream-like feature seen west of Mrk 463E that extends in the general direction of Mrk 463W in the NUV intensity map also appears in the NIR intensity map. This reinforces the probability that this is a real structure and not an observational artifact of the FOC.

Because the NUV and NIR maps have the same pixel size and were properly aligned, it is possible to subtract one from the other. We did this to obtain the excess NUV map that we show in Fig. 6. It is a worthwhile exercise as the NUV excess can be used to determine whether the UV light could be attributed to recent star formation (which, in turn, can be linked to evolutionary processes in the host galaxy) or a direct consequence of the AGN activity (Fabian 1989). Our map clearly shows that the latter explanation is correct in the case of Mrk 463E: The NUV excess perfectly matches the polar wind geometry. It is thus solid evidence advocating the reprocessing of the the UV-NIR continuum emission from the illuminating source (i.e., the nucleus) onto the northern winds. Additionally, it indicates that the northern winds are located in front of the galactic plane of the host, in a similar fashion as NGC 1068 (Kishimoto 1999). The southern winds are very likely obscured by the dusty content of the host galaxy. It is interesting to note that there is a deficit of UV photons precisely at the base of the northern wind. A correlation of this NUV-excess map to radio maps of the parsec-scale jets might provide additional information to constrain the location of the nucleus more precisely.

4.2. Correlation with the Chandra 2-8 keV observation

In the high-energy domain, where photon fluxes are weaker, it is hard to acquire high-resolution images. This is detrimental because arcsecond X-ray imaging could provide a wealth of information about black hole growth with time, through mergers (like Mrk 463E) or AGN fueling (Mushotzky et al. 2019). Fortunately, the Chandra X-ray Observatory was pointed toward this system in June 2004 (ObsId 4913) and took full advantage of its Advanced CCD Imaging Spectrometer (ACIS). The observation allowed the first, firm identification of the two nuclei as Seyfert-2 galaxies (Bianchi et al. 2008).

Similarly to the WFPC2 case, we downloaded and reduced the data in order to overlay the soft X-ray emission onto the FOC map. The result of this exercise is presented in Fig. 7. The alignment was more complex as the spatial resolution of the Chandra map (0.492″ × 0.492″) is one order of magnitude lower than that of the HST/FOC. We used the fact that both AGNs (Mrk 463E and Mrk 463W) were observed by Chandra to align the two objects with the NUV map. Ultimately, the peak of X-ray emission is clearly consistent with the peak of the NUV flux in the first arcsecond around the hidden nucleus, but subtle details are elusive. Moreover, even though the X-rays are more extended than the NUV emission, the two nuclei are well separated in the Chandra map. This confirms that the Mrk 463E HST/FOC image is not contaminated by the western nucleus.

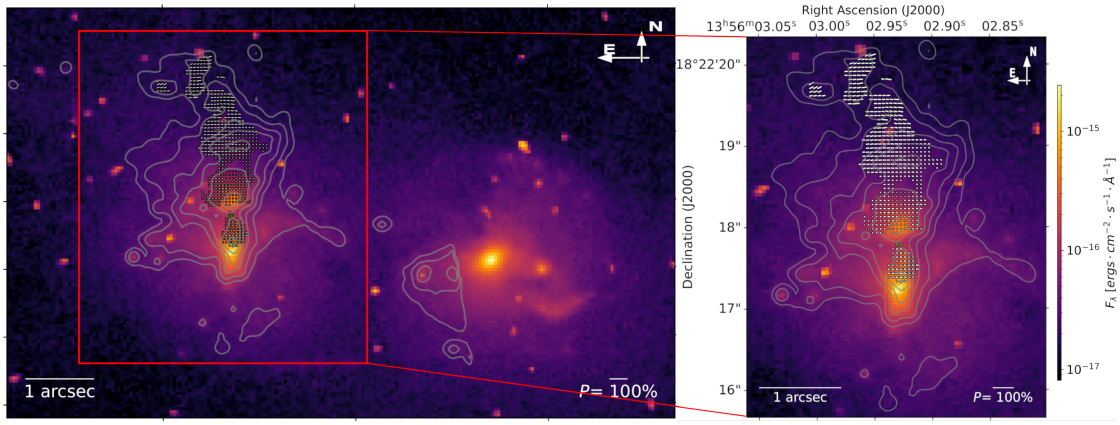

Fig. 5. WFPC2 observation of Mrk 463, overlaid with the polarization vectors obtained from the FOC observation analysis. The NIR and NUV maps are both aligned on similar-looking features around the nucleus of Mrk 463E.

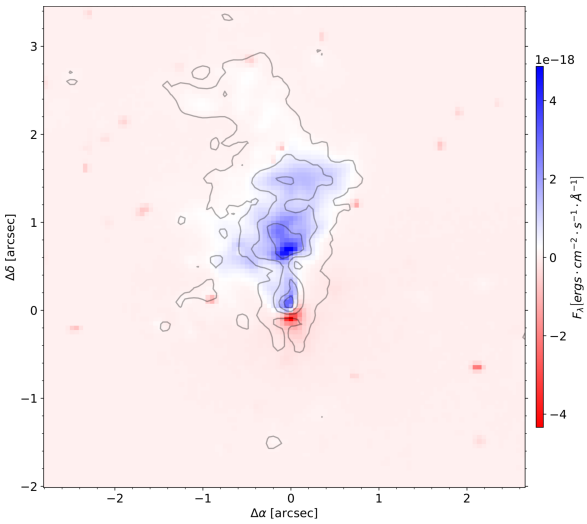

Fig. 6. HST/WFPC2 image at 7996 Å subtracted from the HST/FOC image at 3404 Å. Both maps were binned to a 0.05″ pixel size and aligned on similar-looking features. The contours display the level of the NUV-polarized flux density, correlated with the polar wind of the AGN.

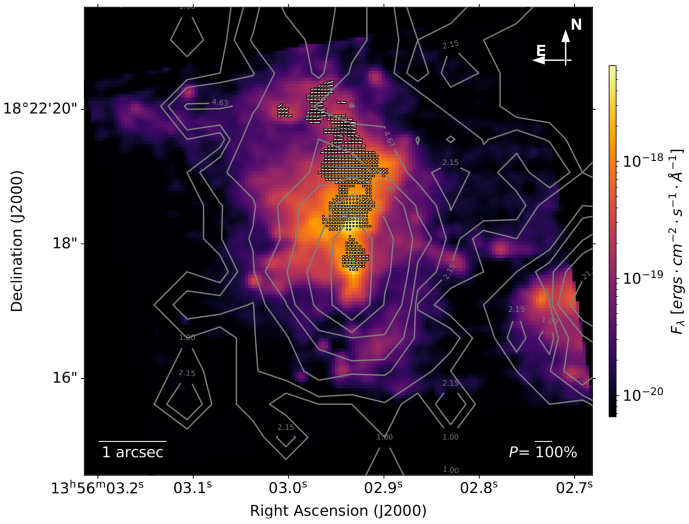

Fig. 7. Chandra observation of Mrk 463E, shown with contours overlaid on the FOC observation analysis, showing the NUV flux density and polarization map. The contours correspond to every tenth percentile of the maximum Chandra counts.

5. Discussion

5.1. A streamer connecting Mrk 463E and Mrk 463W?

Through the sharp contrast of the total intensity of the HST/FOC NUV map against the diffuse background, we observed an elongated faint source that extends from the northern wind of Mrk 463E toward the southwest, in the general direction of Mrk 463W (see Fig. 1). This stream has an NIR counterpart in the WFPC2 observation with a slightly lower contrast than in the FOC map. This NIR/NUV comparison allows us to confirm that the stream has a pronounced curvature that connects to the base of the northern wind of Mrk 463E (see Fig. 5). For this reason, it might be thought that it is a stream of gas and dust that is linked to the past encounter between Mrk 463E and Mrk 463W, and not a filament related to the AGN winds.

In order to analyze this structure more closely, we integrated the polarization of this stream in the HST/FOC image using a simulated slit of 0.35″ × 1.15″ at an angle of 67° , so that it received a maximum of flux from the stream itself and as little pollution as possible from the AGN wind and the background. The polarization is detected at the 89% confidence level and is reported in Sect. 3.3 and Table 1. It indicates an electric vector polarization angle of $\Psi^6 \sim 133°$. This polarization angle is inconsistent with the hypothesis that the AGN nuclei (either Mrk 463E or Mrk 463W) are the primary sources of radiation scattering onto the stream. For example, for a scattering target located at the center of our extraction region, the line orthogonal to the direction toward the hidden nucleus of Mrk 463E would correspond to a polarization angle of 41°.

The low confidence in this measure serves only for a speculative discussion. The polarization from this potential stream is thus uncorrelated to the AGN (otherwise, it would probably also have appeared on the NUV-excess map). The fact that the magnetic vector, orthogonal to the measured electric vector polarization angle, is roughly aligned with the stream direction suggests that the origin of the polarization could very well be dichroic absorption from the host starlight of Mrk 463E (or within the stream itself) in the foreground dusty stream (we recall that Mrk 463E is situated farther away from us than Mrk 463W). The integrated polarization angle could then highlight the large kiloparsec-scale ordered magnetic field in the stream. Gas

streamers with highly compressed magnetic fields like this have been found in interacting galaxies both in radio (Drzazga et al. 2011) and far-IR observations (Lopez-Rodriguez et al. 2023). Although the measurement only has a confidence level of 89%, the pieces of evidence that indicate that a real stream connects the two nuclei are intriguing. New IR and radio observations are mandatory to explore this feature in more depth.

5.2. What do the winds tell us?

The polarization map allows us to study the two components of the polar winds, that is, the NLR and the ionization cone, the former of which is visible in total intensity and the latter in polarized flux density. Both are clearly delimited geometrically against the background emission, so that we can measure their half-opening angle in Fig. 3. The NLR shows a half-opening angle of ∼36° with respect to the jet axis of the system, which agrees with the first results from Tremonti et al. (1996), while the ionization cone that is revealed in polarized flux density, only has a half-opening angle of ∼15°. Inside the ionized cone, the polarization angle stays uniform at ∼90° with a very small dispersion. On average, high-polarization degrees are well correlated with peaks in the total intensity, which can be related to higher cloud densities. We report almost no polarization around the bottleneck between the two NUV hot spots (the region between the white lines noted "high 1" and "low 2" in Fig. 3). This could result from kinematics constraints inside the wind, a sudden lack of scatter material in this region, or from a variation in the past ejection activity of Mrk 463E. In the latter case, continuum photons may scatter on the radio jet between two periods of mass ejection, which would explain the bridge-like feature in the total and polarized flux densities. High-resolution imaging of the radio jets is required to confirm this hypothesis.

The excess map in Fig. 6 shows that the northern wind is above the plane of the host galaxy. This result is confirmed by the observed negative velocity with respect to the systemic velocity obtained from mapping the [OIII] 5007 Å line emission (see Fig. 12 (left) in Treister et al. 2018). However, the inclination of the winds is unknown. We may still try to infer the global inclination of the AGN through polarimetry. When we assume that the NUV radiation we measured only consists of radiation scattered by free electrons and that no other diluting component exists, we can then deduce the scattering angle from the nuclei toward the line of sight within the framework of single scattering,

$$P = \frac{1-\mu^2}{1+\mu^2}, \tag{1}$$

where $\mu = \cos\theta$ and θ is the scattering angle. This relation works well when the size of the scattering target is small enough compared with the distance to the illuminating source (Kishimoto 1999). Considering only pixels with $[S/N]_P \geq 5$ in region 3 (see Fig. 4), we find an averaged P of 20.8 ± 0.6%, which translates into two solutions for θ : $\theta_1 = 144.1 \pm 0.5°$ and $\theta_2 = 35.9 \pm 0.5°$ (uncertainties on θ were propagated from the previous formula). As a result, we can conclude that Mrk 463E is probably inclined by about 90°−35.9° = 54.1° (rounded to a value of 55° for simplicity) with respect to the jet axis. This is well within the expected range of inclinations for a type 2 object (Marin 2014, 2016).

Additionally, the shape of the winds that is revealed in total intensity and polarimetry shows three regions (regions 1, 2, and 3 in Fig. 4) that resemble compact clusters of material that are illuminated by the hidden nuclei and are separated by regions of flux underdensity. This might correspond to periods of massive polar ejection spaced by periods of calmer nuclear activity. These gaps between the different clumps of matter are particularly visible in the polarized flux map between regions 1 and 2 (see Fig. 2). Based on the tentative value for the inclination of the AGN, we can estimate the duration of the activity periods that led to massive polar ejection. Based on our analysis, we assume an inclination angle toward the observer of $\theta_{\rm incl} = 55°$ and a uniform wind velocity $V = 350\,{\rm km\,s^{-1}}$ (Treister et al. 2018). According to the hypothesis that the origin of the wind is the nucleus (Joh et al. 2021), whose location is determined by the cone apexes in Fig. 3, we can deduce the propagation time,

$$T = \frac{a_z \cdot A^{\rm obs}}{V \cdot \cos\theta_{\rm incl}} \simeq 5.0455 \cdot A^{\rm obs}\,{\rm Myr}, \tag{2}$$

where a_z is the conversion factor of the angular to the linear size for Mrk 463E at $z = 0.05132$ in the standard ΛCDM cosmology, and $A^{\rm obs}$ is the observed angular size on the HST/FOC map in arcseconds. We report the results in Table 2. From our analysis, we deduce that the clouds in regions 1, 2, and 3 in Fig. 4 were ejected from the nuclei about 4.3, 7.6, and 11.2 Myr ago, respectively. These three clouds display similar ejection duty cycles, with a massive ejection lasting for 2.3 Myr and 1.1 Myr of a quiet state in between. These orders of magnitude are representative of typical AGN duty cycles such as estimated by Turner (2018), Biava et al. (2021), or Maccagni et al. (2021), for example.

Table 2. Angular distance from the nucleus and propagation time.

Region	Angular size (arcsec)	Propagation time (Myr)
Lower 1	0.64	3.21
Higher 1	1.08	5.43
Lower 2	1.27	6.38
Higher 2	1.75	8.84
Lower 3	2.00	10.08
Higher 3	2.44	12.30

Notes. Distances are taken to the inner and outer edges of each cloud. Their corresponding propagation times are computed from Eq. (2). Each distance is taken from the apex of the cone to the associated region indicated in Fig. 3.

6. Conclusion

In this second paper of our series, we made use of the general pipeline to reduce the HST/FOC archival data presented in Barnouin et al. (2023) to analyze a previously unpublished dataset. The archived observation of Mrk 463E are a true forgotten treasure and a great illustration of the strength of high spatial resolution NUV polarimetry. The strong polarized flux from the source enabled us to study the NLR extensively and granted us an improved estimate of the location of the nucleus. It lies farther south than what was previously suggested (estimated coordinates: 13h56m02.91s, 18°22′16.6″).

This high angular resolution polarization map also gave a tight estimate of the AGN inclination angle, which we found to be about 55°. We also measured the polar wind half-opening angle between 15° (in polarization) and 35° (in total intensity). The observed polarization agrees well with previous spectropolarimetric studies of Mrk 463E and calls for additional IR studies of the stream-like feature (the gas streamer) between the two

interacting nuclei of the system. This analysis can further be completed with high-resolution radio imaging of the jets to better understand their interaction with the observed NLR.

Acknowledgements. TB and FM would like to acknowledge the support of the CNRS, the University of Strasbourg, the PNHE and PNCG. This work was supported by the "Programme National des Hautes Énergies" (PNHE) and the "Programme National de Cosmologie et Galaxies (PNCG)" of CNRS/INSU co-funded by CNRS/IN2P3, CNRS/INP, CEA and CNES. E.L.-R. is supported by the NASA/DLR Stratospheric Observatory for Infrared Astronomy (SOFIA) under the 08_0012 Program. SOFIA is jointly operated by the Universities Space Research Association,Inc.(USRA), under NASA contract NNA17BF53C, and the Deutsches SOFIA Institut (DSI) under DLR contract 50OK0901 to the University of Stuttgart. E.L.-R. is supported by the NASA Astrophysics Decadal Survey Precursor Science (ADSPS) Program (NNH22ZDA001N-ADSPS) with ID 22-ADSPS22-0009 and agreement number 80NSSC23K1585.

References

Abazajian, K. N., Adelman-McCarthy, J. K., Agüeros, M. A., et al. 2009, ApJS, 182, 543
Antonucci, R. 1993, ARA&A, 31, 473
Antonucci, R. R. J., & Miller, J. S. 1985, ApJ, 297, 621
Barnes, J. E., & Hernquist, L. E. 1991, ApJ, 370, L65
Barnouin, T., Marin, F., Lopez-Rodriguez, E., Huber, L., & Kishimoto, M. 2023, A&A, 678, A143
Bianchi, S., Chiaberge, M., Piconcelli, E., Guainazzi, M., & Matt, G. 2008, MNRAS, 386, 105
Biava, N., Brienza, M., Bonafede, A., et al. 2021, A&A, 650, A170
Capelo, P. R., Dotti, M., Volonteri, M., et al. 2017, MNRAS, 469, 4437
Capetti, A., Macchetto, F., Axon, D. J., Sparks, W. B., & Boksenberg, A. 1995, ApJ, 452, L87
Chatzichristou, E. T., & Vanderriest, C. 1995, A&A, 298, 343
Di Matteo, T., Springel, V., & Hernquist, L. 2005, Nature, 433, 604
Drzazga, R. T., Chyży, K. T., Jurusik, W., & Wiórkiewicz, K. 2011, A&A, 533, A22
Event Horizon Telescope Collaboration (Akiyama, K., et al.) 2019, ApJ, 875, L1
Event Horizon Telescope Collaboration (Akiyama, K., et al.) 2022, ApJ, 930, L12
Fabian, A. C. 1989, MNRAS, 238, 41P
Hopkins, P. F., Hernquist, L., Cox, T. J., et al. 2006, ApJS, 163, 1
Hutchings, J. B., & Neff, S. G. 1989, AJ, 97, 1306
IAU 1973, Trans. Int. Astron. Union, 15, 165
Joh, K., Nagao, T., Wada, K., Terao, K., & Yamashita, T. 2021, PASJ, 73, 1152
Kishimoto, M. 1999, ApJ, 518, 676
Kukula, M. J., Ghosh, T., Pedlar, A., & Schilizzi, R. T. 1999, ApJ, 518, 117
Lavaux, G., & Hudson, M. J. 2011, MNRAS, 416, 2840
Lopez-Rodriguez, E., Borlaff, A. S., Beck, R., et al. 2023, ApJ, 942, L13
Maccagni, F. M., Serra, P., Gaspari, M., et al. 2021, A&A, 656, A45
Marin, F. 2014, MNRAS, 441, 551
Marin, F. 2016, MNRAS, 460, 3679
Mazzarella, J. M., Gaume, R. A., Soifer, B. T., et al. 1991, AJ, 102, 1241
Miller, J. S., & Goodrich, R. W. 1990, ApJ, 355, 456
Miller, J. S., Goodrich, R. W., & Mathews, W. G. 1991, ApJ, 378, 47
Mullaney, J. R., Alexander, D. M., Fine, S., et al. 2013, MNRAS, 433, 622
Mushotzky, R., Aird, J., Barger, A. J., et al. 2019, BAAS, 51, 107
Neff, S. G., & Ulvestad, J. S. 1988, AJ, 96, 841
Oke, J. B., & Sargent, W. L. W. 1968, ApJ, 151, 807
Sanders, D. B., & Mirabel, I. F. 1996, ARA&A, 34, 749
Sanders, D. B., Soifer, B. T., Elias, J. H., et al. 1988, ApJ, 325, 74
Shuder, J. M., & Osterbrock, D. E. 1981, ApJ, 250, 55
Simmons, J. F. L., & Stewart, B. G. 1985, A&A, 142, 100
Tran, H. D. 1995a, ApJ, 440, 565
Tran, H. D. 1995b, ApJ, 440, 578
Tran, H. D. 1995c, ApJ, 440, 597
Treister, E., Schawinski, K., Urry, C. M., & Simmons, B. D. 2012, ApJ, 758, L39
Treister, E., Privon, G. C., Sartori, L. F., et al. 2018, ApJ, 854, 83
Tremonti, C. A., Uomoto, A., Antonucci, R. R. J., et al. 1996, BAAS, 28, 1287
Turner, R. J. 2018, MNRAS, 476, 2522
Unger, S. W., Pedlar, A., Booler, R. V., & Harrison, B. A. 1986, MNRAS, 219, 387
Uomoto, A., Caganoff, S., Ford, H. C., et al. 1993, AJ, 105, 1308
Volonteri, M., Pfister, H., Beckmann, R., et al. 2022, MNRAS, 514, 640
Walker, M. F. 1968, AJ, 73, 854
Wang, C., Wang, J., Dadina, M., et al. 2024, ApJ, 962, 188
Watanabe, M., Nagata, T., Sato, S., Nakaya, H., & Hough, J. H. 2003, ApJ, 591, 714
Wilson, A. S. 1996, Vistas Astron., 40, 63
Yamada, S., Ueda, Y., Oda, S., et al. 2018, ApJ, 858, 106
Young, S., Hough, J. H., Efstathiou, A., et al. 1996, MNRAS, 281, 1206

Appendix A: Confidence level for the polarization degree.

We propose a two parameters confidence level for the polarization degree that differ from the $4-\sigma_P$ detection level proposed by Simmons & Stewart (1985). This method relies solely on the scalar Stokes Q and U fluxes, computed in units of counts per second throughout the whole pipeline. These can be modeled along with gaussian noise. As per definition of the Stokes fluxes, we compute the polarization degree as $P = \sqrt{q^2+u^2}$, with $q = Q/I$ and $u = U/I$ the normalized Stokes Q and U fluxes. We define the confidence at which we detect the polarization on the χ^2 statistic on the normalized Stokes Q and U fluxes with their associated normalized uncertainties:

$$\chi^2 = \frac{q^2}{{\sigma_q}^2} + \frac{u^2}{{\sigma_u}^2} \tag{A.1}$$

The confidence level is computed on the cumulative distributive function for χ^2 with two parameters of interest

$$CL = CDF(\chi^2, 2) = 1 - e^{-\frac{1}{2}\chi^2} \tag{A.2}$$

We compare the $3-\sigma_P$ and $4-\sigma_P$ detection levels on the flux density map of Mrk 463E in Fig. A.1. In our case, the 99% confidence level as defined in Eq. A.2 encompass a region less restrictive than the $4-\sigma_P$ level, but slightly more restrictive than the $3-\sigma_P$ level, in accordance with the suggestion by Simmons & Stewart (1985).

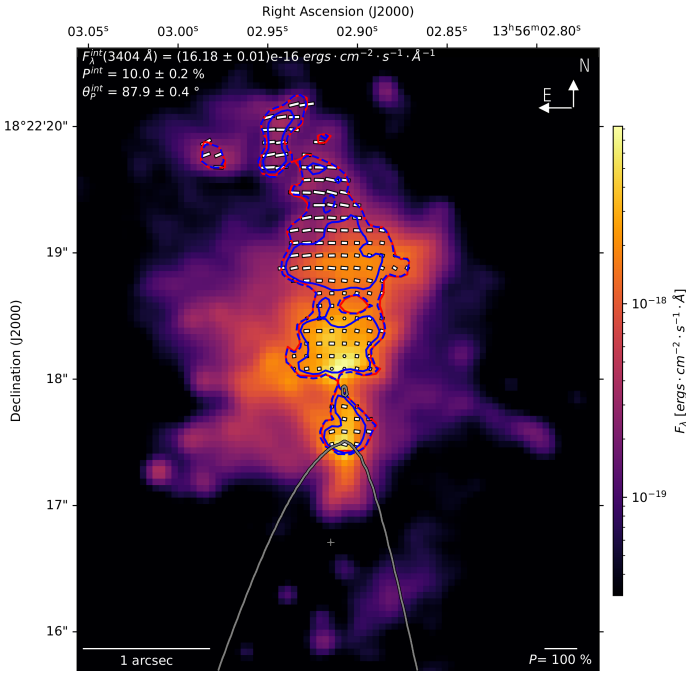

Fig. A.1. Comparison of the determination of a detection between levels of signal to noise ratio in debiased polarization degree in blue for $3-\sigma_P$ (dashed line) and $4-\sigma_P$ (solid line) with the Stokes Q and U fluxes confidence level defined in Eq. A.2 in red. The gray contour and position are the 99% confidence level and best guess for the position of the center of emission by minimizing Eq. B.1.

Appendix B: Localization of the emission center

The single scattering of a photon from a point source onto an ionized polar outflow produces polarization with an electrical polarization angle perpendicular to the direction to the source. Based on the full uncertainties on the computed polarization angle, we evaluate the confidence with which the detected polarization is consistent with point-source scattering.

$$\chi^2(x_c, y_c) = \sum_{i \in A} \frac{\left[\theta_{\rm PA}(i) - \theta_{\rm ideal}(i; x_c, y_c)\right]^2}{{\sigma_{\rm PA}(i)}^2} \tag{B.1}$$

with A a valid (≥ 5 sigmas) subset of polarization vectors, $\theta_{\rm PA}$ the observed polarization angle and $\sigma_{\rm PA}$ its associated full uncertainty as defined in Barnouin et al.(2023, Eq 21). For any vector i at pixel coordinates x_i, y_i, the ideal centrosymmetric PA for a center of emission at pixel coordinates x_c, y_c is:

$$\theta_{\rm ideal}(i; x_c, y_c) = \arctan\left(\frac{y_c - y_i}{x_c - x_i}\right) \tag{B.2}$$

By minimizing the value of χ^2, we find our best estimation for the location of the nucleus in the hypothesis of single scattering onto ionized medium, assuming for scattering on a single plane. We show the 99% confidence level contour and the emission center that minimize Eq. B.1 with A the set of vectors with a polarization confidence greater than 99%. Both the contour and best estimate agree with the estimation from the wind cones openings in Sect. 3.1 and Fig. 3. We note that the 99% contour does not exclude for a nucleus location as previously suggested in the literature (Uomoto et al. 1993) but this hypothesis remains marginal.